

1 A theory of evolutionary dynamics on any complex population
2 structure: spatial architecture as a suppressor of selection in the
3 stem cell niches of the bone marrow

4 Yang Ping Kuo¹, César Nombela Arrieta², and Oana Carja *¹

5 ¹Computational Biology Department, School of Computer Science, Carnegie Mellon
6 University, Pittsburgh, PA, USA

7 ²Department of Medical Oncology and Hematology, University and University Hospital
8 Zurich, Zurich, Switzerland

9 **Abstract**

10
11 How the spatial arrangement of a population shapes its evolutionary dynamics has been of long-
12 standing interest in population genetics. Most previous studies assume a small number of demes or
13 symmetrical structures that, most often, act as well-mixed populations. Other studies use network the-
14 ory to study more heterogeneous spatial structures, however they usually assume small, regular networks,
15 or strong constraints on the strength of selection considered. Here we build network generation algo-
16 rithms, conduct evolutionary simulations and derive general analytic approximations for probabilities of
17 fixation in populations with complex spatial structure. We build a unifying evolutionary theory across
18 network families and derive the relevant selective parameter, which is a combination of network statistics,
19 predictive of evolutionary dynamics. We also illustrate how to link this theory with novel datasets of
20 spatial organisation and use recent imaging data to build the cellular spatial networks of the stem cell
21 niches of the bone marrow. Across a wide variety of parameters, we find these networks to be strong
22 suppressors of selection, delaying mutation accumulation in this tissue. We also find that decreases in
23 stem cell population size also decrease the suppression strength of the tissue spatial structure.

*To whom correspondence should be addressed. Email: oana.carja@gmail.com or yangpink@andrew.cmu.edu.

²⁴ **Keywords:**

²⁵ population structure; network theory; evolution on networks; amplifiers of selection; suppressors of selection;
²⁶ rates of mutation accumulation; stem cell spatial structure

²⁷

Introduction

²⁸ Novel microfluidics and organoid technologies (Simian and Bissell, 2017; Holloway et al., 2019) allow us to
²⁹ start building biological scaffolds that control the spatial topology of a molecular or cellular population.
³⁰ In order to make full use of these innovations, we need a rigorous theory of how the spatial structure of
³¹ a population shapes its future evolutionary dynamics. This will allow us to design structures that either
³² amplify the selective benefit and spread of beneficial mutations, or structures that suppress the spread of
³³ deleterious variants.

³⁴ There is a large body of literature in population genetics theory studying the role of population structure
³⁵ in shaping evolutionary outcome, starting from the classic 1975 paper of Slatkin and Maruyama (Slatkin
³⁶ and Maruyama, 1975). However, most previous modeling approaches that incorporate spatial patterns of
³⁷ variation usually only assume a few demes (patches) and symmetrical structures (Wright, 1943; Kimura and
³⁸ Weiss, 1964; Carja et al., 2014), simple topologies that can be embedded into two-dimensional continuous
³⁹ Euclidean space. In most cases, these simple topologies do not change fixation probabilities and rates
⁴⁰ of evolution compared to well-mixed populations (Maruyama, 1970; Slatkin, 1981). These symmetrical
⁴¹ structures fundamentally fail to capture the complex pattern of interaction and the variance in local selection
⁴² pressure present in natural populations as well as in emerging spatial cellular and molecular atlases (Regev
⁴³ et al., 2018; Snyder et al., 2019; Uhlen et al., 2010).

⁴⁴ Studying more complex topologies, ones for which there exists no homeomorphism to the well-behaved
⁴⁵ two-dimensional Euclidian space, becomes a much harder mathematical problem. These topologies can be
⁴⁶ represented using networks and we can use the mathematical formalism of the Moran birth-death process on
⁴⁷ graphs (Lieberman et al., 2005; Carja and Creanza, 2019), to explore how spatially-structured patterns of
⁴⁸ interaction and replacement drive the composition of populations and shape the outcome of the evolutionary
⁴⁹ process. Under these models, a population of individuals is located on nodes of a graph and the links of a
⁵⁰ node indicate the neighboring nodes that can be replaced by its offspring (Lieberman et al., 2005). Graph
⁵¹ theory has been successfully used to study patterns of spatial variation and interaction across a wide range of
⁵² scientific fields, from the social sciences to brain science (Centola, 2010; Bassett and Bullmore, 2006; Nowak,

53 2006b; Sood and Redner, 2005).

54 Initial studies on very small graphs observe large differences between networks in the fixation probability
55 of new mutants, compared to well-mixed populations (Lieberman et al., 2005; Hindersin and Traulsen, 2015),
56 a marked departure from previous deme-based models. Some graphs are suppressors of selection, graphs
57 that reduce the fixation probability of advantageous mutations, while increasing it for deleterious mutants
58 (Lieberman et al., 2005; Hindersin and Traulsen, 2015; Hindersin et al., 2016a). Other graphs can be classified
59 as amplifiers, increasing rates of evolution. One of the first general results, the isothermal theorem, states
60 that in graphs where the propensity for change in each node is exactly the same, the fixation probabilities
61 of new mutations are the same as in well-mixed populations. The assumptions of the isothermal theorem,
62 however, sit on a knife edge; make small perturbations to the network structure and the assumptions no
63 longer hold (Lieberman et al., 2005). While these initial studies hint at the promise of graph theoretical
64 approaches, analytic results with predictive power have been very difficult to derive. Most prior results either
65 rely on very small networks (where build and solve time scale exponentially with population size, making
66 them unsuitable for the study of networks of more than 30 nodes (Hindersin et al., 2016a)) or invading
67 mutants in the limit of neutrality, results that do not scale to generality (McAvoy and Allen, 2021). What
68 are the probabilities of fixation for a new mutation as a function of where and when it appears in much
69 larger, and more biologically-realistic spatial networks?

70 Here, we develop an analytic approach that gives us the ability to systematically study probabilities of
71 fixation on larger, heterogeneous spatial structures and identify graph properties that control suppression or
72 amplification of selection, either leading evolution to a stand-still or accelerating the evolutionary process.
73 Linking network topology to evolutionary dynamics is complicated by the fact that networks differ in many
74 structural properties. We build graph generation computational methods that allow the ability to systemat-
75 ically tune network statistics and study their role on probabilities and times to fixation for new mutations in
76 the population, mathematical proxies for evolutionary outcome. Our algorithms combine simulated anneal-
77 ing procedures and degree preserving edge swapping (Taylor, 1981) to continuously tune network properties
78 one at a time, while keeping other properties constant. This allows us to fully understand the role of specific
79 network parameters, as well as translate the meaning of the relevant parameters for any given network,
80 across different graph-families.

81 Using our simulations and analytical approximations, we find that knowing the degree distribution alone
82 is not enough to determine the fixation probabilities and times to fixation since graphs with the same degree
83 distribution, but different mixing pattern can exhibit very different evolutionary outcome. Importantly, we

84 analytically derive the relevant selective parameter for a given network, without making restrictive assumptions
85 on network type, size or selective advantage of the new invading variant.

86 In addition to the purely theoretical interest of the questions presented above, we also showcase how our
87 theoretical results can be used to analyze rates of evolution in the stem cell populations of the bone marrow
88 (Klein and Simons, 2011; Tomasetti et al., 2017). We use recent imaging data sets (Couto et al., 2018;
89 Gomariz et al., 2018) to build the spatial stem networks of the bone marrow and we find that these networks
90 are strong suppressors of selection, across a wide range of parameter choices and regardless of the type of
91 the assumed birth-death process. Moreover, we find decreasing suppression with decreasing population size,
92 hinting at a potential decrease in the suppressive properties of the spatial structure as individuals age.

93 Model

94 We use a Moran-type model to describe changes in allele frequencies in a finite population of constant size
95 N . Each individual's genotype is defined by a single biallelic locus A/a , which controls the individual's
96 reproductive fitness. An individual with the A allele is assumed to have fitness one, while an individual with
97 allele a has assigned fitness $(1 + s)$.

98 We use the structure of a graph to represent the spatial structure of the population. Every individual
99 occupies a node in the graph, while the edges between nodes represent the local pattern of replacement.
100 At every generation, we update the allele frequencies using two different update scenarios (**Figure 1A**).
101 In the first update scenario, we assume reproduction occurs before death (the Birth-death *Bd* scenario).
102 At every time step, we first select one individual for reproduction, with probability proportional to fitness,
103 from the entire population. We then randomly select one of its neighbors for death and vacate the node for
104 the new offspring. In the second update scenario, denoted as the death-Birth *dB* update, we first select a
105 node at random from the population to be vacated and then choose one of its neighbors for reproduction,
106 with probability proportional to fitness. Note that selection happens only when choosing the individual to
107 reproduce. This means that, in the Birth-death update, the individuals compete globally, at the population
108 level, while in the death-Birth update, the selection step is local, the competing individuals are only the
109 neighbors of the node randomly chosen for death. Due to these differences in global versus local competition,
110 the two update rules have been shown to lead to drastically different evolutionary dynamics (Lieberman et al.,
111 2005; Hindersin and Traulsen, 2015).

112 The graph structure therefore becomes a mathematical proxy for the spatial topology or the population

113 structure of replacement: individuals reproduce locally, and their offspring spread to neighboring nodes
114 connected by an edge. The graphs we consider here are unweighted and undirected. Initially, we assume
115 the population fixed on the wild-type *A* allele. We introduce one mutant *a* individual at a random node at
116 time $t = 0$ and we ignore subsequent mutation. Under this model, the population will eventually reach a
117 monomorphic state where individuals of the same *A/a* allele occupy all nodes in the graph. We study the
118 probability of fixation of the invading allele *a* as a function of the population size N , the selective coefficient
119 of the new mutant *s* and importantly, the topological features of the network spatial structure. Our goal is
120 to systematically study the role of the network structure in shaping rates of evolution by directly comparing
121 these probabilities of fixation with the equivalent probabilities in a well-mixed population.

122 Linking network topology to evolutionary dynamics is complicated by the fact that networks differ in
123 many structural properties and tuning parameters independent of others is not a trivial problem. To identify
124 the relevant graph properties that either speed up or suppress adaptation through shaping probabilities and
125 times to fixation of new mutants in the population, we characterize graphs through the lens of their main
126 two components: the nodes and the edges. We can therefore think of graph properties as either node- or
127 edge-centric. The main property of a node is the node degree (the number of neighbors the node is linked to)
128 and the node degree distribution becomes an important global network property (Newman, 2003). Graph
129 edges, on the other hand, can be categorized based on the type of nodes they connect and how often they
130 connect nodes of different degrees. The mixing pattern of a graph (also called graph assortativity) is a global
131 edge-centric graph descriptor that informs on the frequencies of each edge type (Newman, 2002).

132 To begin with, we use random graph generators and construct graphs that span the known graph families
133 (Barabási and Albert, 1999; Holme and Kim, 2002; Watts and Strogatz, 1998; Waxman, 1988; Penrose
134 et al., 2003; Erdős and Rényi, 1960; Masuda et al., 2005). This ensures that our results are generalizable
135 across graph families and graph properties (**Figure 1B**). Two graph generator families we highlight are the
136 Barabasi-Albert model of preferential attachment and the generalized random geometric model.

137 In preferential attachment (PA) graphs, each network starts with a single node and nodes are added
138 sequentially until the population reaches size N . Each new node is added to the network and connected
139 to other individuals with a probability proportional to the individual's current degree to the power of a
140 given parameter β . By adjusting the number of edges added each step (m) and the power of preferential
141 attachment (β), this family of graphs allows for straightforward independent tuning of the moments of the
142 degree distribution. Parameter m is the only parameter of the model that controls the first moment of
143 the degree distribution. Parameter β controls the shape of the distribution, with the distribution being

144 exponential when $\beta = 0$, stretched exponential when $0 < \beta < 1$, and power law when $\beta = 1$ (Krapivsky
 145 et al., 2000). When the power of preferential attachment $\beta = 1$, PA graphs exhibit the scale-free property
 146 (Barabási and Albert, 1999) and that is why PA graphs are often used as a model to study the spread of
 147 information or cultural norms (Creanza et al., 2017). In contrast, for generalized random geometric graphs
 148 (Waxman, 1988; Penrose et al., 2003), nodes have spatial positions randomly drawn from a probability
 149 distribution to model spatially homogeneous populations (using the uniform distribution) or populations
 150 with heterogeneous spatial density (using the normal distribution). Once the spatial locations of the nodes
 151 are determined, the generating algorithm iterates through all pairs of nodes. An edge is created between two
 152 nodes using a probability distribution based on pair-wise distance. Here we use an exponential distribution
 153 (the resulting graphs are known as Waxman graphs) and a heavy-side function where we connect two nodes
 154 if the distance is below a predefined threshold (denoted as random geometric graphs).

155 However, existing graph generating methods do not allow for the separate tuning of the degree distribution
 156 and the node degree mixing pattern. For example, in PA graphs, one can smoothly change the shape of
 157 the degree distribution by changing the power of preferential attachment β . However, if we change this
 158 preference of connection to high degree nodes, we inevitably also change the graph's mixing pattern and
 159 cannot independently study its role in amplifying or suppressing selection.

160 To allow for tuning of mixing patterns, independent of the degree distribution, we implement a sampling
 161 network generation algorithm based on simulated annealing (**Figure 1C**). The algorithm relies on a degree
 162 swapping operation on graphs (Taylor, 1981) and runs for a preset number of time steps. The algorithm
 163 works as follows: at every time step, two random edges are selected. Let us denote them by A-B and
 164 C-D. The two edges are broken and rewired to form A-C and B-D. The degree distribution of the graph
 165 is preserved, while other properties such as the mixing pattern of nodes are changed. Thus, we can use
 166 the edge swapping operation to find graphs with extreme graph properties from all possible graphs of fixed
 167 degree distribution. The algorithm can take any graph as input. We use degree Pearson correlation r to
 168 measure the mixing pattern in the graph (Newman, 2002). Parameter r ranges from -1 to 1, with positive r
 169 for networks where nodes with similar degrees are preferentially connected, and negative degree correlation
 170 for networks where high degree nodes preferentially form edges with low degree nodes.

171 If the goal is to find the graph that maximizes the degree correlation, we accept an edge swap according
 172 to the criterion

$$\text{Uniform}[0, 1] < \min \left(1, \exp^{-\gamma(r_{\text{after}} - r_{\text{before}})} \right) \quad (1)$$

173 and reject the step otherwise. Here, $1/\gamma$ is the annealing temperature that controls how stringent the criterion

174 must be and is decreased as the simulation proceeds. Intermediate graphs are periodically saved and we use
175 the heuristic outlined in Gkantsidis et al. (2003) to periodically check that the graph is fully connected. This
176 algorithm yields a set of graphs spanning a range of possible degree correlations, thus allowing us to study
177 the effects of mixing pattern on evolutionary dynamics, without changes to the graph degree distribution.

178 Once the network structure is set, we use ensembles of at least 10,000 Monte Carlo simulations, as well
179 as analytic approaches as described in the next section, to compute the probabilities of fixation of the new
180 allele a .

181 Results

182 We study the probability of fixation of a new invader mutation a with fitness $(1 + s)$ that appears in a
183 random initial node of the network and compare it with the equivalent probabilities of fixation in well-mixed
184 populations. We start by obtaining analytic approximations for the dB (death-Birth) update model and
185 then discuss the important differences specific for the Bd (Birth-death) update rule. Intuitively, the dB
186 dynamics applies when the evolutionary update are driven by available space being freed up, followed by
187 local competition among the neighbors, whereas the Bd dynamics applies in cases where competition happens
188 globally, but replacement is driven by the local pattern of interaction.

189 Analytic description

190 We begin by presenting the main ideas of our analytic approximation for the probability of fixation of the a
191 allele. For the complete mathematical treatment, please see the **Supplementary Material**. Previous ana-
192 lytic approaches have either made use of the adjacency matrix of the network (which uniquely identifies the
193 graph) and its associated transition probabilities (Hindersin et al., 2016a) or assumed that the evolutionary
194 dynamics are in the limit of neutrality and a vanishing selection coefficient s (if weak selection is assumed,
195 the probability of fixation can be approximated by treating it as the linear perturbation to the continuous
196 coalesce, the dual of the Moran process under neutrality) (McAvoy and Allen, 2021; Allen et al., 2017). The
197 former approach can provide closed form solutions for the fixation probability of a , but becomes intractable
198 for large networks since it tracks a Moran process with 2^N states and the algorithm build and solve time both
199 grow exponentially with population size (even for $N = 23$ nodes it can take several minutes (Hindersin et al.,
200 2016a)). The latter approach reduces the problem from exponential to polynomial complexity in population
201 size N (McAvoy and Allen, 2021; Allen et al., 2017), however it performs poorly as we move away from the

202 neutrality limit for the a allele (**Supplementary Figure S1** and **S2**).

203 The approach we take here is to use the node degree distribution, and only keep track of the mutant
 204 frequencies x_i at all N_i nodes of the same degree d_i . Let $D = \{d_1, d_2, \dots, d_i, \dots\}$ represent the set of all
 205 possible node degrees. While the degree distribution might not uniquely represent the network and some of
 206 the graph information is lost, this approach nonetheless greatly reduces the number of possible states in the
 207 Moran model (Ohtsuki et al., 2007; Sood and Redner, 2005). We denote the frequency of nodes of degree d_i
 208 in the population by p_i . To model node degree mixing, we use p_{ij} to denote the probability that a node of
 209 degree d_i is connected to a node of degree d_j . The probability of fixation of allele a is then approximated
 210 using the diffusion approximation (Kimura, 1962; Crow et al., 1970).

211 At every time point, x_i , the frequency of the mutant at nodes of degree d_i , increases by $1/N_i$ with
 212 probability T_i^+ and decreases by $1/N_i$ with probability T_i^- . We can write

$$\begin{aligned} T_i^+ &= \frac{1+s}{W} \sum_{j \in D} p_j p_{ji} x_j (1 - x_i) \\ T_i^- &= \frac{1}{W} \sum_{j \in D} p_j p_{ji} (1 - x_j) x_i, \end{aligned} \quad (2)$$

213 where W is the mean fitness of the individuals in the population.

214 We use these transition probabilities to find the mean and covariance of the change in x_i per unit time
 215 and use the backward Kolmogorov equation (Crow et al., 1970) to find the probability of fixation of the a
 216 allele for any initial mutant frequency $P(\vec{x})$:

$$\sum_i \left(\frac{T_i^+ - T_i^-}{p_i} \frac{\partial P}{\partial x_i} + \frac{1}{2} \frac{T_i^+ + T_i^-}{N p_i^2} \frac{\partial^2 P}{\partial x_i^2} \right) - \frac{1}{2} \sum_{i,k} \frac{(T_i^+ - T_i^-)(T_k^+ - T_k^-)}{N p_i p_k} \frac{\partial^2 P}{\partial x_i \partial x_k} = 0. \quad (3)$$

217 Here, the coefficient for the linear differential operator is quadratic in x_i and the coefficient for the
 218 quadratic differential operator is quartic in x_i .

219 By using singular perturbation to linearize the coefficients of the differential equation (Gavrilets and
 220 Gibson, 2002), the solution to the partial differential equation in (3) for the Birth-death update model can
 221 be approximated by:

$$\sum_{i,j \in D} p_i p_{ij} \left(\frac{1}{2p_i^2} ((1+s)x_j + x_i) \frac{\partial^2 P}{\partial x_i^2} + \frac{1}{p_i} ((1+s)x_j - x_i) \frac{\partial P}{\partial x_i} \right) = 0. \quad (4)$$

222 The death-Birth process shares a similar equation, given by

$$\sum_{i,j \in D} p_j p_{ji} \left(\frac{1}{2p_i^2} ((1+s)x_j + x_i) \frac{\partial^2 P}{\partial x_i^2} + \frac{1}{p_i} ((1+s)x_j - x_i) \frac{\partial P}{\partial x_i} \right) = 0. \quad (5)$$

223 The only difference between the two equations is the change from $p_i p_{ij}$ to $p_j p_{ji}$. The solution for the Bd
224 process can then be written as

$$P(\vec{x}) = \frac{1 - \exp \left\{ -N \sum_{i \in D} p_i A_{Bd,i} x_i \right\}}{1 - \exp \left\{ -N \sum_{i \in D} p_i A_{Bd,i} \right\}}. \quad (6)$$

225 We can compute A_{Bd} by solving the following system of quadratic equations

$$\sum_{j \in D} \left[(1+s) A_{Bd,j}^2 p_i p_{ij} + A_{Bd,i}^2 p_j p_{ji} - 2(1+s) A_{Bd,j} p_i p_{ij} + 2A_{Bd,i} p_j p_{ji} \right] = 0, \quad \forall i \quad (7)$$

226 while for dB update processes we need to solve

$$\sum_{j \in D} \left[(1+s) A_{dB,j}^2 p_j p_{ji} + A_{dB,i}^2 p_i p_{ij} - 2(1+s) A_{dB,j} p_j p_{ji} + 2A_{dB,i} p_i p_{ij} \right] = 0, \quad \forall i. \quad (8)$$

227 In the death-Birth process, the contribution to the fixation probability due to the degree distribution is
228 on the order of the selection coefficient s , while the contribution due to degree mixing is on the order of s^2 .
229 Therefore, knowing the degree distribution of the graph gives a good approximation to the probability of
230 fixation, for weak s . Assuming $s \sim \frac{1}{N}$, the probability of fixation can be approximated as

$$P_{dB} = \frac{1 - e^{-\alpha_{dB}s/(1+s/2)}}{1 - e^{-\alpha_{dB}Ns/(1+s/2)}}, \quad \text{where } \alpha_{dB} = \frac{\langle d \rangle^2}{\langle d^2 \rangle}. \quad (9)$$

231 Here, $\langle d \rangle = \sum p_i d_i$ and $\langle d^2 \rangle = \sum p_i d_i^2$ are the first and second moment of the degree distribution. This
232 selection suppression or amplification factor α_{dB} can be used to measure how much the probability of fixation
233 differs from that of well-mixed populations. If $\alpha = 1$, the probability of fixation is identical to well-mixed
234 populations. Graphs with $\alpha > 1$ are amplifiers and $\alpha < 1$ are suppressors. In the limit of weak selection,
235 equation (9) becomes $\frac{1-e^{-s}}{1-e^{-Ns}}$ for the well-mixed population (Ewens, 2004; Nowak, 2006a).

236 Our approximation shows that, for sufficiently weak selection, α_{dB} , the suppression parameter for dB
237 processes, is a function of the first and second moments of the degree distribution alone.

238 Solving equations (7) and (8), we show the accuracy of the analytic approximation in **Figure 2** using

239 preferential attachment PA graphs. As the mean of the degree distribution increases, probability and time
 240 of fixation increase for the death-Birth process (and decrease for the Birth-death process) towards the well-
 241 mixed population limit. This makes intuitive sense: as the mean degree increases, the graph structure
 242 approaches that of a well-mixed population. In contrast, as the variance of the degree distribution increases,
 243 while keeping the mean constant, probabilities and times to fixation decrease monotonically for the dB
 244 process, and increase for the Bd process. The variance measures how heterogeneous the nodes are. At
 245 variance zero, all the nodes in the graph have the same number of neighbors, which means the graph is
 246 isothermal and the fixation probability is the same as that of well-mixed populations.

247 Using the approximation in (9) for the death-Birth dB process, we show the probability of fixation of
 248 a new mutation a across multiple graph families in **Figure 3A**. As the effective selection parameter α
 249 increases, the fixation probability increases, reaching and crossing the well-mixed line when α equals to one.
 250 Intuitively, α quantifies the interplay between the mean and variance of the degree distribution, between
 251 how well-connected the nodes are and the network node heterogeneity.

252

253 The evolutionary role of graph mixing pattern

254 For the Birth-death process, unlike the case of the death-Birth process where the effects of mixing pattern
 255 can be ignored under weak selection, network degree distribution and mixing pattern both contribute to
 256 the new mutation's fixation probability. Similar to the death-Birth process, the contribution to the fixation
 257 probability due to degree distribution is again on the order of the selection coefficient of the new mutation s .
 258 However, in contrast to the death-Birth process, the graph mixing pattern has the same order of magnitude
 259 contribution as the graph degree distribution. Under selection $s \sim \frac{1}{N}$, the probability of fixation can be
 260 approximated as

$$P_{Bd} = \frac{1 - e^{-\alpha_{Bd}s/(1+s/2)}}{1 - e^{-\alpha_{Bd}Ns/(1+s/2)}}, \quad \text{where } \alpha_{Bd} = \left(\langle d^{-1} \rangle \sum_{i,j \in D} p_j p_{ji} d_i^{-1} \right) \left(\sum_{i,j \in D} p_j p_{ji} d_i^{-2} \right)^{-1}. \quad (10)$$

261 Here, $\langle d^{-1} \rangle = \sum p_i d_i^{-1}$ is the first inverse moment of the degree distribution.

262 For the Birth-death process, the α_{Bd} selection factor can be written as a function of parameters of the
 263 network wiring pattern and properties of its degree distribution. This approximation is shown in **Figure**
 264 **3B**, alongside the results of Monte Carlo simulations. The fixation probability increases as the selection
 265 parameter α increases, with lower values for random geometric graphs and higher selection amplification for

266 the preferential attachment graph family.

267 To understand the underlying network properties controlling evolutionary dynamics of new mutations,
268 we need an intuitive understanding of the amplification factor in equation (10). The inverse moment $\langle d^{-1} \rangle$
269 quantifies the shape of the degree distribution, while the rest of the parameters in equation (10) can be
270 thought of as parameters that measure the graph's assortativity or mixing pattern (Newman, 2002). A
271 graph is assortative when a node of degree d_i preferentially attaches to other nodes of a degree similar to
272 d_i . A graph is called disassortative when the number of edges that connects nodes of degree d_i and nodes of
273 dissimilar degree is higher than the expected number in randomly mixing graphs. Consider an edge swapping
274 operation on a graph that breaks two edges: one between two nodes of degree d_i and one between two nodes
275 of degree d_j . Two edges that connect node of degree d_i and degree d_j are formed from the stubs. If d_i and d_j
276 are dissimilar, such a rewiring step reduces the graph's assortativity. Assuming the population size is large,
277 the change in the α_{Bd} amplification factor can be written as

$$\Delta\alpha_{Bd} \sim \left(\frac{1}{d_i} - \frac{1}{d_j} \right)^2 \left(\frac{1}{d_i} + \frac{1}{d_j} - \frac{\mu_2}{\mu_1} \right), \text{ where } \mu_1 = \sum_{i,j \in D} p_j p_{ji} d_i^{-1} \text{ and } \mu_2 = \sum_{i,j \in D} p_j p_{ji} d_i^{-2}. \quad (11)$$

278 The magnitude of the change depends on the difference between the reciprocals of the degrees. If new
279 edges are created between nodes of very dissimilar degrees, the change in the fixation probability can be
280 significant. Since the change depends on the reciprocal, nodes of low degree have a disproportional effect
281 on the change in amplification. The upper bound of μ_2/μ_1 is $1/d_{min}$, where d_{min} is the smallest degree of
282 the graph. This means that if either d_i or d_j is close to the lowest degree, α_{Bd} is guaranteed to increase. In
283 other words, the probability of fixation increases when there are more edges connecting nodes of low degrees
284 to nodes of high degrees (disassortative graphs). An example of this is the star network, one of the strongest
285 amplifiers for undirected graphs (Pavlogiannis et al., 2017; Möller et al., 2019; Tkadlec et al., 2019). A star
286 graph consists of a few nodes forming the center, while the rest of the nodes connect to the center nodes and
287 form the vertices of the star. As a consequence, the nodes at the center have high degrees, while the rest tend
288 to have significantly smaller degree, and the only edge type in the graph is between nodes of very different
289 degrees. This type of graphs have the highest disassortativity, and strongest amplification of selection.

290 We can use this intuition to also explain the relative location of graph families in **Figure 3B**. Preferential
291 attachment networks tend to be graphs with low assortativity (high disassortativity), with many hub-and-
292 spoke structures (lower degree nodes connected to high degree nodes) and thus strong amplifiers. In contrast,
293 normal geometric graphs with non-uniform spatial density tend to have high assortativity and thus tend to

294 suppress the force of selection. This is due to the fact that nodes in high-density areas tend to be closer to
295 each other and, assuming the density function is relatively smooth, neighbors tend to have similar degrees.
296 Similarly, nodes in low spatial density areas tend to have few neighbors (low degrees), and so do their
297 neighbors. Therefore, in spatial graphs with nonuniform spatial density, nodes are connected with neighbors
298 of similar degree. This explains the suppression effect of this network family.

299 Since knowing the degree distribution alone is not enough to determine the fixation probability and
300 amplification parameter for the Birth-death process, to illustrate the effects of assortativity and mixing
301 pattern on fixation probabilities without the influence of degree distribution and graph generating method,
302 we use edge swap operations to sample graphs with different mixing patterns, while keeping the degree
303 distribution the same. We use graphs generated from different generating methods as input graphs to ensure
304 generalization across graph families. For the same degree distribution, the spread of values for the fixation
305 probability due to the effect of degree mixing can be substantial (**Figure 4A**). Here, all dots of the same
306 color represent graphs from the same starting graph family and are altered by the edge swap sampling
307 method with different end mixing patterns. We use the variance of the degree distribution as a measure for
308 the shape of the distribution. Although the mean degree is not shown, dots of the same color share the same
309 mean.

310 We use degree Pearson correlation r as a measure of the mixing pattern in the graph. We maximize
311 and minimize the degree correlation to obtain an ensemble of graphs with the same degree distribution
312 but different mixing pattern. When $r = 1$, the network has perfect assortative mixing patterns, while
313 $r = -1$ corresponds to the case of a disassortative network. The contribution of the mixing pattern in the
314 amplification constant in equation (10) is also a measure of assortativity (**Figure 4B**). r and α_{Bd} have a
315 negative correlation, as expected. For graphs with the same degree distribution, the graphs that have low
316 assortativity (high α_{Bd}) have a higher probability of fixation (**Figure 4C**). The difference between **Figure**
317 **4C** and **Figure 3B** is that in **4C** we keep the degree distribution constant. Therefore, both node types and
318 edge types in a graph both contribute to evolutionary dynamics on the graph structure.

319 Increased suppression of selection in large populations

320 While it has been previously claimed that under the Birth-death process most graphs are amplifiers of
321 selection (Hindersin and Traulsen, 2015), our results above show that a large fraction of Birth-death graphs
322 are suppressors of selection. The discrepancy in the results is due to the different population sizes considered.
323 Due to computational and analytic limitations, previous studies consider very small population sizes of under

324 $N = 30$ individuals. In this section, we study the effects of population size on fixation probabilities using
325 two types of graphs: star graphs, known to be one of the strongest undirected amplifiers, and detour graphs,
326 strong suppressors (Möller et al., 2019; Tkadlec et al., 2019).

327 A detour graph consists of a completely connected central cluster and a cycle part (see **Figure 5**). These
328 graphs have a low probability of fixation due to their high assortativity, since the graphs only have two
329 edges connecting nodes of different degrees. We show that the fixation probability depends on the size of
330 the central cluster, i.e. the length of the detour. To find the cluster size that minimizes the probability of
331 fixation, we use the solution to the diffusion equation (47) in the **Supplementary Material**, derived using
332 regular perturbation (Zhivotovsky and Feldman, 1993):

$$P_{Bd} \approx \frac{1}{N} + s \sum_{ij} p_i p_j A_{ij}, \quad (12)$$

333 where A_{ij} satisfy the following system of linear equations

$$\begin{aligned} p_j p_{ji} \left(-\frac{1}{\langle d^{-1} \rangle d_i} + 2 \frac{A_{ii}}{N} \right) - 2 \sum_k p_i p_j p_{jk} A_{ki} + 2 \sum_k p_j p_k p_{ki} A_{ij} \\ + p_i p_{ij} \left(-\frac{1}{\langle d^{-1} \rangle d_j} + 2 \frac{A_{jj}}{N} \right) - 2 \sum_k p_j p_i p_{ik} A_{kj} + 2 \sum_k p_i p_k p_{kj} A_{ij} = 0. \end{aligned} \quad (13)$$

334 The size of this system of equations is $|D|(|D| + 1)/2$, where $|D|$ is the number of unique degrees in the
335 graph. Since a detour graph has only two types of degrees, we only need to solve a system of 3 equations for
336 A_{11} , A_{12} , and A_{22} . The only variable that influences the probability of fixation in the detour graphs is the
337 length of the detour. We plot the difference in probabilities of fixation for detour graphs of different sizes
338 and the well-mixed population against the length of the detour in **Figure 5A**. When detour length equals
339 zero, we have the complete graph where the difference in the probability of fixation is zero. Since detour
340 length is maximized in a ring graph, the probability of fixation initially decreases as the length of the detour
341 is increased, reaching a minimum, before increasing towards the well-mixed control. It can also be observed
342 that the minimum decreases with population size. The regular perturbation approximation is used instead
343 of equation (10) since, while the approximation predicts the magnitude of suppression on detour graphs,
344 the minima are shifted slightly to the left towards well-mixed. Mathematically, this is due to the fact that
345 singular perturbation deviates from the solution of the diffusion equation when the exchange of individuals
346 between two sub-populations is weak (Whitlock and Gomulkiewicz, 2005).

347 The star graphs and the detour graphs constitute limiting structures for the range of probabilities of

fixation for undirected graphs under sufficiently weak selection (**Figure 5B**). The difference in probability of fixation between the detour graph and a well-mixed population is close to zero when graph size is small, however it decreases sharply as population size increases. This explains why strong suppressors are prevalent in large populations, but rarely observed in small populations. Although we did not rigorously prove that detour graphs serve as the lower bound for the probability of fixation under the Birth-death update, this is empirically observed in graphs of small size (Möller et al., 2019). It is reasonable to assume the existence of large graphs that have stronger suppression, but this only reinforces our point that suppressors are more prevalent in larger populations. The result is particularly biologically interesting. Imagine populations with individuals fixed in space, such as species in an ecosystem or cells in biological tissues. These spatial populations can be reasonably approximated by random geometric or Waxman graphs. As shown in the previous section, these types of populations are likely to be suppressors under the Birth-death update. If the size of the population were to decrease (for example, environmental catastrophes or injury and aging of tissues), not only will the force of drift increase in the population, but also the suppressive capability of the population against the invasion of beneficial mutation will be compromised. This could lead to increased likelihood of beneficial mutations propagating in the population (and potential rescue the population from extinction), or increased rate of accumulation of deleterious driver mutations that initiate neoplasms.

Application to mutation accumulation in hematopoietic stem cell populations

We show how the theory developed above can be linked to novel datasets of spatial localization and specifically, be used for the study of rates of mutation accumulation in the hematopoietic stem cell (HSC) population of the bone marrow. Hematopoietic stem cells reside in specialized micro-environments, or niches, where distinct mesenchymal cells, the vasculature, and differentiated hematopoietic cells interact to regulate stem cell maintenance and differentiation (Morrison and Scadden, 2014; Baccin et al., 2020). These niches are fixed in location and number, with heterogeneous spatial structure, and stem cells are in constant competition for niche occupancy (Celso and Scadden, 2011; Glait-Santar et al., 2015).

New innovations in imaging techniques and our ability to process these images at scale offer unprecedented opportunities to study how the spatial heterogeneity of stem cell niches shape tissue evolutionary dynamics. Just as demographic surveys can reveal the rates at which a contagious disease can spread through a spatially heterogeneous population, these imaging datasets allow us to quantify cellular and molecular patterns of spatial variation and study how these topologies shape evolutionary dynamics. We use published datasets that provide the spatial location of hematopoietic stem and progenitor cells in four samples of mouse tibia

378 (Coutu et al., 2018) and the spatial locations of 8 bone marrow samples of CXCL12-abundant reticular cells
379 (which critically modulate hematopoiesis at various levels, including hematopoietic stem cell maintenance),
380 each with two images of two anatomically distinct regions (the diaphysis and the metaphysis), in total 16
381 cellular populations (Gomariz et al., 2018).

382 Adult hematopoietic stem cells are known to divide symmetrically, whereby a mother stem cell either
383 divides into two differentiated daughter cells or two undifferentiated stem cells (Wu et al., 2007; Hofer et al.,
384 2020). The two modes of symmetric division are analogous to birth and death in a population described by
385 the Moran process. We build the networks of stem cell niches and use the inferred spatial topologies to infer
386 the accumulation rate of driver mutations, the main cause of cancer in cycling tissues (Klein and Simons,
387 2011). Every HSC niche constitutes a node in the graph and an edge is added between two nodes if the
388 distance between them is less than a cut-off radius, similar to the generation of a random geometric graph.
389 The samples vary in dimensions, number of cells, and segmentation techniques. We normalize the data by
390 expressing the distance in units of the average distance between shortest pairs of cells ($62.72\text{ }\mu\text{m}$ for HSC).
391 One resulting network is shown in **Figure 6A**. For illustration purposes, for the network shown, the cutoff
392 distance is set to $300\mu\text{m}$ ($4.78\times$ the distance between shortest pairs).

393 We analyze evolutionary dynamics on networks generated using cut-off radii ranging from 2 to 20 times
394 the average distance between shortest pairs. The difference in probabilities of fixation, compared to those
395 in well-mixed populations, is plotted against the population size in **Figures 6B** (Birth-death update) and
396 **6C** (death-Birth update). The fixation probabilities are either close to or lower than that of the well-mixed,
397 except networks generated using two times the distance between the shortest pair as the cut-off radius. The
398 color dots are the results using a cut-off distance of 15, which is the closest to our estimated biological
399 interaction range. We interpret the cut-off distance as the maximum distance a HSC could travel in its
400 entire lifespan. Live-animal tracking of individual hematopoietic stem cells in their niche showed MFG
401 cells, a largely quiescent population with long-term self-renewal capability, displacing an average distance
402 of $8.69\mu\text{m}$ in a 2.5 hour period (Christodoulou et al., 2020). HSCs have median replication time (the time
403 when 50% of HSCs have divided) of 1.7 weeks (Abkowitz et al., 2000). During homeostasis, the rate of
404 replication should balance the rate of depletion. This leads to the estimated interaction range of $1028\mu\text{m}$
405 which corresponds to $16.4\times$ the distance between the shortest pairs.

406 We show that geometric graphs constructed from a non-uniform spatial distribution of individuals are
407 likely to result in an assortative mixing pattern, hence we find suppression of selection in the hematopoietic
408 stem cell populations, invariant to the underlying update process (compare panels **6B** and **6C**). We also

409 construct networks with a probabilistic connection function (Waxman, 1988) and observe no qualitative
410 difference.

411 Our results also show that the strength of suppression increases as the stem cell population size increases
412 and the fixation probability shows a negative correlation with population size (Pearson correlation of -0.687
413 and p-value of 0.001). A similar conclusion is reached with most other cut-off distances (see examples of
414 cut-off distances 10 and 20 in the **Supplementary Figure S6**), as well as other mutant selection coefficients
415 (see examples of 5% and 10% fitness increases in **Supplementary Figure S7**). A previous study by Dingli
416 and Pacheco (2006) predicts that the total number of active stem cells in mammals scales with body mass
417 with exponent 3/4. Assuming similar bone marrow tissue architecture in systems with more stem cells,
418 suppression of selection is predicted to be amplified in larger mammals. This observation could partially
419 explain the observed reduction in cancer incidence in large organisms as stated by Peto's paradox (Caulin
420 and Maley, 2011). This also implies that processes such as injury or aging, that lead to reduced stem cell
421 and niche count, could lead to the increased likelihood of beneficial mutations propagating in the population
422 and an increased risk of developing cumulative diseases of aging, such as cancer.

423 Discussion

424 Graphs represent a powerful tool to mathematically represent a population's structure of spread or interaction
425 and to ask how properties of this structure shape the balance of evolutionary forces. However, obtaining
426 closed form solutions for evolutionary dynamics on graphs has been particularly difficult. Here we introduce
427 new theoretical and computational methods to rigorously study the role of graph topology on shaping
428 evolutionary dynamics. We focus on parameters of the degree distribution and the graph mixing pattern
429 because these distributions inform on graph-wide properties of the fundamental building blocks of a network:
430 the nodes and the edges.

431 We show that the probability of fixation of a new mutation appearing on a random node can be approx-
432 imated by solving a system of quadratic equations with number of variables depending on the number of
433 degrees in the graph, which in most practical cases is efficient, even in large populations. By tuning the first
434 moments of the degree distribution independently of each other, we analyze how the mean and variance in
435 degree change probabilities and times to fixation. For example, we show that the probability of fixation under
436 the Birth-death update increases monotonically as a function of the variance of the degree distribution. This
437 is because the parameter that controls degree heterogeneity also controls the mixing pattern of the graph,

438 by changing the connection bias towards nodes of higher degree.

439 Moreover, we write the relevant selective parameter of suppression or amplification (α_{dB} and α_{Bd}),
440 predictive of whether the network is an amplifier or suppressor of selection. While for the death-Birth
441 process, this constant depends on properties of the degree distribution, for the Birth-death process, this
442 constant is composed of parameters of both the mixing pattern and the degree distribution of the graph.
443 If degree distribution is held constant, increasing the amplification parameter corresponds to increasing
444 the disassortativity of the graph. Or reversely, increasing the disassortativity of a network increases the
445 probabilities of fixation monotonically across multiple random graph families. For the death-Birth process,
446 increasing disassortativity also increases the fixation probability, but only when selection is larger than order
447 of $1/N$.

448 The limitation of this approach is that it ignores higher-order organizations of the network, such as
449 community structures and network motifs and assumes that nodes of the same degree are topologically
450 similar. Furthermore, our approach averages the assortativity of individual nodes over the entire graph
451 and an example where this approach would not work is for a graph consisting of two parts connected by a
452 few edges, one highly assortative, and one highly disassortative. The graph would be treated as neutrally
453 assortative and this would lead to incorrect prediction of the fixation probability.

454 We also show that, contrary to prior empirical observations on small graphs (Hindersin and Traulsen,
455 2015), the Birth-death process can also be a strong suppressor of selection and not just an amplifier. For
456 example, detour graphs are a class of graphs that show strong suppression under the Birth-death process.
457 These graphs are extremely assortative and the magnitude of the suppression is shown to depend on the
458 detour size. We analytically find the optimal suppression sizes of the detour graphs for any given population
459 size, and empirically show that the magnitude of maximum suppression decreases with population size. Since
460 the lower bound of fixation probability decreases as population size increases, there are hints at the possible
461 existence of an arbitrarily strong suppressor that neglects selective advantages in a large population. In
462 biological settings, such as spatially complex ecosystems or cells in biological tissues, large populations are
463 therefore more likely to be suppressors under the Birth-death update. If an event were to decrease the size
464 of the population (for example, environmental catastrophes that lead to the destruction of forests or injury
465 and aging of tissues), not only will the force of drift increase in the population, but also the suppressive
466 capability of the population against the invasion of beneficial mutation will be compromised. One caveat
467 is that this magnitude of suppression also depends on the strength of selection, and these topologies can
468 transition from suppressor to amplifier given large enough selection pressure.

469 In rapidly cycling tissues, tissue maintenance and repair are coordinated by stem cells, which are routinely
470 stochastically lost and replaced in the population (Klein and Simons, 2011) and thus instrumental for studying
471 rates of evolution and mutation accumulation (Tomasetti et al., 2017). Previous theoretical studies on
472 the population dynamics of stem cells either ignore the structure of the tissue, consider the topology of small
473 populations of stem cells (Hindersin et al., 2016b; Lopez-Garcia et al., 2010), or assume cells are arranged
474 in lattices where every node has the same degree (Klein et al., 2010). By analyzing recent imaging data on
475 the spatial organization of hematopoietic stem cells in the bone marrow, we show that stem cell populations
476 are organized to minimize fixation probabilities of new mutants spreading through the population.

477 While our focus here is to understand the evolutionary properties of the architecture of the stem cell
478 niches, our approach makes many more questions ripe for exploration. For example, in a recent study,
479 Watson et al. (2020) use a well-mixed model to estimate mutation accumulation and selection coefficients in
480 clonal hematopoiesis. Similarly, Heyde et al. (2021) inferred division time and mutational fitness effects from
481 variant allele frequency (VAF) data using a well-mixed Moran model, and found that increased stem cell
482 proliferation expedites somatic evolution. Our results highlight that spatial heterogeneity can reduce the rate
483 at which driver mutations spread through the population and suggest that using a well-mixed model to fit
484 data produced by a spatially-structured population can potentially underestimate the strength of selection on
485 somatic variants. Furthermore, in growing tumors, discrepancies can arise when sampling does not capture
486 a uniform representation of the population, since over- or under-representation of mutations in the VAF
487 distributions due to spatial effects can be mistaken as signatures of selection (Chkhaidze et al., 2019). The
488 theory we present here can also be extended to study the evolutionary dynamics of spatially heterogeneous
489 tumor populations (Anderson and Chaplain, 1998; Waclaw et al., 2015; Lewinsohn et al., 2023; Drost et al.,
490 2017; Tuveson and Clevers, 2019).

491 Further work on how network properties shape evolutionary dynamics will also help us understand how
492 to construct spatial structures in the limit of either suppression or amplification across various biological
493 systems, natural or artificial. This would allow controlled suppression against the spread of unwanted variants
494 and delay of population collapse. Reversely, we could also use population structure as a screening tool for
495 faster amplification of newly discovered beneficial mutations or optimized protein complexes for medical or
496 industrial applications.

497 Data and code availability

498 The XXx data used in this paper is

499 **Code availability**

500 Source code that allows for the reproduction of the simulations and results presented here can be found
501 on Github at the following link: <https://github.com/yangpingkuo/Suppressor-of-selection-in-the-stem-cell-niches-of-the-bone-marrow>.
502

503 **References**

- 504 Janis L Abkowitz, Daniela Golinelli, David E Harrison, and Peter Guttorp. In vivo kinetics of murine
505 hemopoietic stem cells. *Blood, The Journal of the American Society of Hematology*, 96(10):3399–3405,
506 2000.
- 507 Benjamin Allen, Gabor Lippner, Yu-Ting Chen, Babak Fotouhi, Naghmeh Momeni, Shing-Tung Yau, and
508 Martin A Nowak. Evolutionary dynamics on any population structure. *Nature*, 544(7649):227–230, 2017.
- 509 Alexander RA Anderson and Mark AJ Chaplain. Continuous and discrete mathematical models of tumor-
510 induced angiogenesis. *Bulletin of mathematical biology*, 60(5):857–899, 1998.
- 511 Chiara Baccin, Jude Al-Sabah, Lars Velten, Patrick M Helbling, Florian Grünschläger, Pablo Hernández-
512 Malmierca, César Nombela-Arrieta, Lars M Steinmetz, Andreas Trumpp, and Simon Haas. Combined
513 single-cell and spatial transcriptomics reveal the molecular, cellular and spatial bone marrow niche orga-
514 nization. *Nature cell biology*, 22(1):38–48, 2020.
- 515 Albert-László Barabási and Réka Albert. Emergence of scaling in random networks. *Science*, 286(5439):
516 509–512, 1999.
- 517 Danielle Smith Bassett and Ed Bullmore. Small-world brain networks. *The Neuroscientist*, 12(6):512–523,
518 2006.
- 519 Oana Carja and Nicole Creanza. The evolutionary advantage of cultural memory on heterogeneous contact
520 networks. *Theoretical Population Biology*, 129:118 – 125, 2019.
- 521 Oana Carja, Uri Liberman, and Marcus W Feldman. Evolution in changing environments: Modifiers of
522 mutation, recombination, and migration. *Proceedings of the National Academy of Sciences*, 111(50):17935–
523 17940, 2014.
- 524 Aleah F Caulin and Carlo C Maley. Peto’s paradox: evolution’s prescription for cancer prevention. *Trends
525* in ecology & evolution

- 526 Cristina Lo Celso and David T Scadden. The haematopoietic stem cell niche at a glance. *Journal of cell*
527 *science*, 124(21):3529–3535, 2011.
- 528 Damon Centola. The spread of behavior in an online social network experiment. *Science*, 329(5996):1194–
529 1197, 2010.
- 530 Ketevan Chkhaidze, Timon Heide, Benjamin Werner, Marc J Williams, Weini Huang, Giulio Caravagna,
531 Trevor A Graham, and Andrea Sottoriva. Spatially constrained tumour growth affects the patterns of
532 clonal selection and neutral drift in cancer genomic data. *PLoS computational biology*, 15(7):e1007243,
533 2019.
- 534 Constantina Christodoulou, Joel A Spencer, Shu-Chi A Yeh, Raphaël Turcotte, Konstantinos D Kokkaliaris,
535 Riccardo Panero, Azucena Ramos, Guoji Guo, Negar Seyedhassantehrani, Tatiana V Esipova, et al. Live-
536 animal imaging of native haematopoietic stem and progenitor cells. *Nature*, 578(7794):278–283, 2020.
- 537 Daniel L Coutu, Konstantinos D Kokkaliaris, Leo Kunz, and Timm Schroeder. Multicolor quantitative
538 confocal imaging cytometry. *Nature methods*, 15(1):39–46, 2018.
- 539 Nicole Creanza, Oren Kolodny, and Marcus W Feldman. Cultural evolutionary theory: How culture evolves
540 and why it matters. *Proceedings of the National Academy of Sciences*, 114(30):7782–7789, 2017.
- 541 James F Crow, Motoo Kimura, et al. An introduction to population genetics theory. *An introduction to
542 population genetics theory*, 1970.
- 543 David Dingli and Jorge M Pacheco. Allometric scaling of the active hematopoietic stem cell pool across
544 mammals. *PLoS One*, 1(1):e2, 2006.
- 545 Jarno Drost, Ruben Van Boxtel, Francis Blokzijl, Tomohiro Mizutani, Nobuo Sasaki, Valentina Sasselli, Joep
546 de Ligt, Sam Behjati, Judith E Grolleman, Tom van Wezel, et al. Use of crispr-modified human stem cell
547 organoids to study the origin of mutational signatures in cancer. *Science*, 358(6360):234–238, 2017.
- 548 Paul Erdős and Alfréd Rényi. On the evolution of random graphs. *Publ. Math. Inst. Hung. Acad. Sci*, 5(1):
549 17–60, 1960.
- 550 Warren John Ewens. *Mathematical population genetics: theoretical introduction*, volume 27. Springer, 2004.
- 551 Sergey Gavrilets and Nathan Gibson. Fixation probabilities in a spatially heterogeneous environment. *Pop-
552 ulation Ecology*, 44(2):51–58, 2002.

- 553 Christos Gkantsidis, Milena Mihail, and Ellen Zegura. The markov chain simulation method for generating
554 connected power law random graphs. *Alenex*, 2003.
- 555 Chen Glait-Santar, Ronan Desmond, Xingmin Feng, Taha Bat, Jichun Chen, Elisabeth Heuston, Benjamin
556 Mizukawa, James C Mulloy, David M Bodine, Andre Laroche, et al. Functional niche competition
557 between normal hematopoietic stem and progenitor cells and myeloid leukemia cells. *Stem Cells*, 33(12):
558 3635–3642, 2015.
- 559 Alvaro Gomariz, Patrick M Helbling, Stephan Isringhausen, Ute Suessbier, Anton Becker, Andreas Boss,
560 Takashi Nagasawa, Grégory Paul, Orcun Goksel, Gábor Székely, et al. Quantitative spatial analysis of
561 haematopoiesis-regulating stromal cells in the bone marrow microenvironment by 3d microscopy. *Nature
562 communications*, 9(1):1–15, 2018.
- 563 Alexander Heyde, David Rohde, Cameron S McAlpine, Shuang Zhang, Friedrich F Hoyer, Jeffrey M Gerold,
564 David Cheek, Yoshiko Iwamoto, Maximilian J Schloss, Katrien Vandoorne, et al. Increased stem cell
565 proliferation in atherosclerosis accelerates clonal hematopoiesis. *Cell*, 184(5):1348–1361, 2021.
- 566 Laura Hindersin and Arne Traulsen. Most undirected random graphs are amplifiers of selection for birth-
567 death dynamics, but suppressors of selection for death-birth dynamics. *PLoS Comput Biol*, 11(11):
568 e1004437, 2015.
- 569 Laura Hindersin, Marius Möller, Arne Traulsen, and Benedikt Bauer. Exact numerical calculation of fixation
570 probability and time on graphs. *Biosystems*, 150:87–91, 2016a.
- 571 Laura Hindersin, Benjamin Werner, David Dingli, and Arne Traulsen. Should tissue structure suppress or
572 amplify selection to minimize cancer risk? *Biology Direct*, 11(1):1–11, 2016b.
- 573 Thomas Hofer, Hans-Reimer Rodewald, Katrin Busch, Ann-Kathrin Fanti, Alessandro Greco, Xi Wang,
574 Qin Zhang, Melania Barile, Hideyuki Oguro, and Sean J Morrison. Hematopoietic stem cells self-renew
575 symmetrically or gradually proceed to differentiation. *bioRxiv*, 2020.
- 576 Emily M. Holloway, Meghan M. Capeling, and Jason R. Spence. Biologically inspired approaches to enhance
577 human organoid complexity. *Development*, 146(8), 2019.
- 578 Petter Holme and Beom Jun Kim. Growing scale-free networks with tunable clustering. *Physical review E*,
579 65(2):026107, 2002.
- 580 Motoo Kimura. On the probability of fixation of mutant genes in a population. *Genetics*, 47(6):713, 1962.

- 581 Motoo Kimura and George H Weiss. The stepping stone model of population structure and the decrease of
582 genetic correlation with distance. *Genetics*, 49(4):561, 1964.
- 583 Allon M Klein and Benjamin D Simons. Universal patterns of stem cell fate in cycling adult tissues. *Devel-
584 opment*, 138(15):3103–3111, 2011.
- 585 Allon M Klein, Toshinori Nakagawa, Rie Ichikawa, Shosei Yoshida, and Benjamin D Simons. Mouse germ
586 line stem cells undergo rapid and stochastic turnover. *Cell stem cell*, 7(2):214–224, 2010.
- 587 Paul L Krapivsky, Sidney Redner, and Francois Leyvraz. Connectivity of growing random networks. *Physical
588 review letters*, 85(21):4629, 2000.
- 589 Maya A Lewinsohn, Trevor Bedford, Nicola F Müller, and Alison F Feder. State-dependent evolutionary
590 models reveal modes of solid tumour growth. *Nature Ecology & Evolution*, 7(4):581–596, 2023.
- 591 Erez Lieberman, Christoph Hauert, and Martin A Nowak. Evolutionary dynamics on graphs. *Nature*, 433
592 (7023):312–316, 2005.
- 593 Carlos Lopez-Garcia, Allon M Klein, Benjamin D Simons, and Douglas J Winton. Intestinal stem cell
594 replacement follows a pattern of neutral drift. *Science*, 330(6005):822–825, 2010.
- 595 Takeo Maruyama. Effective number of alleles in a subdivided population. *Theoretical population biology*, 1
596 (3):273–306, 1970.
- 597 Naoki Masuda, Hiroyoshi Miwa, and Norio Konno. Geographical threshold graphs with small-world and
598 scale-free properties. *Physical Review E*, 71(3):036108, 2005.
- 599 Alex McAvoy and Benjamin Allen. Fixation probabilities in evolutionary dynamics under weak selection.
600 *Journal of Mathematical Biology*, 82(3):14, 2021.
- 601 Marius Möller, Laura Hindersin, and Arne Traulsen. Exploring and mapping the universe of evolutionary
602 graphs identifies structural properties affecting fixation probability and time. *Communications biology*, 2
603 (1):1–9, 2019.
- 604 Sean J Morrison and David T Scadden. The bone marrow niche for haematopoietic stem cells. *Nature*, 505
605 (7483):327–334, 2014.
- 606 Mark EJ Newman. Assortative mixing in networks. *Physical review letters*, 89(20):208701, 2002.

- 607 Mark EJ Newman. The structure and function of complex networks. *SIAM review*, 45(2):167–256, 2003.
- 608 Martin A Nowak. *Evolutionary dynamics: exploring the equations of life*. Harvard university press, 2006a.
- 609 Martin A Nowak. Five rules for the evolution of cooperation. *Science*, 314(5805):1560–1563, 2006b.
- 610 Hisashi Ohtsuki, Jorge M Pacheco, and Martin A Nowak. Evolutionary graph theory: Breaking the symmetry
611 between interaction and replacement. *Journal of Theoretical Biology*, 246(4):681–694, 2007.
- 612 Andreas Pavlogiannis, Josef Tkadlec, Krishnendu Chatterjee, and Martin A Nowak. Amplification on undi-
613 rected population structures: comets beat stars. *Scientific reports*, 7(1):82, 2017.
- 614 Mathew Penrose et al. *Random geometric graphs*, volume 5. Oxford university press, 2003.
- 615 Aviv Regev, Sarah Teichmann, Orit Rozenblatt-Rosen, Michael Stubbington, Kristin Ardlie, Ido Amit, Paola
616 Arlotta, Gary Bader, Christophe Benoist, Moshe Biton, Bernd Bodenmiller, Benoit Bruneau, Peter Camp-
617 bell, Mary Carmichael, Piero Carninci, Leslie Castelo-Soccio, Menna Clatworthy, Hans Clevers, Christian
618 Conrad, Roland Eils, Jeremy Freeman, Lars Fugger, Berthold Goettgens, Daniel Graham, Anna Greka, Nir
619 Hacohen, Muzlifah Haniffa, Ingo Helbig, Robert Heuckeroth, Sekar Kathiresan, Seung Kim, Allon Klein,
620 Bartha Knoppers, Arnold Kriegstein, Eric Lander, Jane Lee, Ed Lein, Sten Linnarsson, Evan Macosko,
621 Sonya MacParland, Robert Majovski, Partha Majumder, John Marioni, Ian McGilvray, Miriam Merad,
622 Musa Mhlanga, Shalin Naik, Martijn Nawijn, Garry Nolan, Benedict Paten, Dana Pe’er, Anthony Philip-
623 pakis, Chris Ponting, Steve Quake, Jayaraj Rajagopal, Nikolaus Rajewsky, Wolf Reik, Jennifer Rood,
624 Kourosh Saeb-Parsy, Herbert Schiller, Steve Scott, Alex Shalek, Ehud Shapiro, Jay Shin, Kenneth Skel-
625 don, Michael Stratton, Jenna Streicher, Henk Stunnenberg, Kai Tan, Deanne Taylor, Adrian Thorogood,
626 Ludovic Vallier, Alexander van Oudenaarden, Fiona Watt, Wilko Weicher, Jonathan Weissman, Andrew
627 Wells, Barbara Wold, Ramnik Xavier, Xiaowei Zhuang, and Human Cell Atlas Organizing Committee.
628 The human cell atlas white paper, 2018.
- 629 Marina Simian and Mina J. Bissell. Organoids: A historical perspective of thinking in three dimensions.
630 *The Journal of Cell Biology*, 216(1):31–40, 2017.
- 631 Montgomery Slatkin. Fixation probabilities and fixation times in a subdivided population. *Evolution*, pages
632 477–488, 1981.
- 633 Montgomery Slatkin and Takeo Maruyama. Genetic drift in a cline. *Genetics*, 81(1):209–222, 1975.

634 Michael P. Snyder, Shin Lin, Amanda Posgai, Mark Atkinson, Aviv Regev, Jennifer Rood, Orit Rozenblatt-
635 Rosen, Leslie Gaffney, Anna Hupalowska, Rahul Satija, Nils Gehlenborg, Jay Shendure, Julia Laskin,
636 Pehr Harbury, Nicholas A. Nystrom, Jonathan C. Silverstein, Ziv Bar-Joseph, Kun Zhang, Katy Börner,
637 Yiing Lin, Richard Conroy, Dena Procaccini, Ananda L. Roy, Ajay Pillai, Marishka Brown, Zorina S.
638 Galis, Long Cai, Cole Trapnell, Dana Jackson, Michael P. Snyder, Garry Nolan, William James Green-
639 leaf, Sylvia Plevritis, Sara Ahadi, Stephanie A. Nevins, Hayan Lee, Christian Martijn Schuerch, Sarah
640 Black, Vishal Gautham Venkataraaman, Ed Esplin, Aaron Horning, Amir Bahmani, Xin Sun, Sanjay
641 Jain, James Hagood, Gloria Pryhuber, Peter Kharchenko, Bernd Bodenmiller, Todd Brusko, Michael
642 Clare-Salzler, Harry Nick, Kevin Otto, Clive Wasserfall, Marda Jorgensen, Maigan Brusko, Sergio Maffio-
643 letti, Richard M. Caprioli, Jeffrey M. Spraggins, Danielle Gutierrez, Nathan Heath Patterson, Elizabeth K.
644 Neumann, Raymond Harris, Mark deCaestecker, Agnes B. Fogo, Raf van de Plas, Ken Lau, Guo-Cheng
645 Yuan, Qian Zhu, Ruben Dries, Peng Yin, Sinem K. Saka, Jocelyn Y. Kishi, Yu Wang, Isabel Goldara-
646 cena, DongHye Ye, Kristin E. Burnum-Johnson, Paul D. Piehowski, Charles Ansong, Ying Zhu, Tushar
647 Desai, Jay Mulye, Peter Chou, Monica Nagendran, Sarah A. Teichmann, Benedict Paten, Robert F. Mur-
648 phy, Jian Ma, Vladimir Yu. Kiselev, Carl Kingsford, Allyson Ricarte, Maria Keays, Sushma A. Akoju,
649 Matthew Ruffalo, Margaret Vella, Chuck McCallum, Leonard E. Cross, Samuel H. Friedman, Randy Hei-
650 land, Bruce Herr, Paul Macklin, Ellen M. Quardokus, Lisel Record, James P. Sluka, Griffin M. Weber,
651 Nicholas A. Nystrom, Jonathan C. Silverstein, Philip D. Blood, Alexander J. Ropelewski, William E.
652 Shirey, Robin M. Scibek, Paula Mabee, W. Christopher Lenhardt, Kimberly Robasky, Stavros Michailidis,
653 John Marioni, Andrew Butler, Tim Stuart, Eyal Fisher, Shila Ghazanfar, Gokcen Eraslan, Tommaso Bian-
654 calani, Eeshit D. Vaishnav, Ananda Roy, Zorina Galis, Pothur Srinivas, Aaron Pawlyk, Salvatore Sechi,
655 Elizabeth Wilder, James Anderson, HuBMAP Consortium, Writing Group, Caltech-UW TMC, Stanford-
656 WashU TMC, UCSD TMC, University of Florida TMC, Vanderbilt University TMC, California Insti-
657 tute of Technology TTD, Harvard TTD, Purdue TTD, Stanford TTD, Visualization HuBMAP Integra-
658 tion, Tools Component Engagement (HIVE) Collaboratory: Carnegie Mellon, Tools Component Harvard
659 Medical School, Mapping Component Indiana University Bloomington, Pittsburgh Supercomputing Cen-
660 ter, Infrastructure University of Pittsburgh, Engagement Component, Collaboration Core University of
661 South Dakota, Mapping Component New York Genome Center, and NIH HuBMAP Working Group. The
662 human body at cellular resolution: the NIH Human Biomolecular Atlas Program. *Nature*, 574(7777):
663 187–192, 2019.

664 Vishal Sood and Sidney Redner. Voter model on heterogeneous graphs. *Physical review letters*, 94(17):

- 665 178701, 2005.
- 666 Richard Taylor. Constrained switchings in graphs. In *Combinatorial Mathematics VIII*, pages 314–336.
667 Springer, 1981.
- 668 Josef Tkadlec, Andreas Pavlogiannis, Krishnendu Chatterjee, and Martin A Nowak. Population structure
669 determines the tradeoff between fixation probability and fixation time. *Communications biology*, 2(1):138,
670 2019.
- 671 Cristian Tomasetti, Lu Li, and Bert Vogelstein. Stem cell divisions, somatic mutations, cancer etiology, and
672 cancer prevention. *Science*, 355(6331):1330–1334, 2017.
- 673 David Tuveson and Hans Clevers. Cancer modeling meets human organoid technology. *Science*, 364(6444):
674 952–955, 2019.
- 675 Mathias Uhlen, Per Oksvold, Linn Fagerberg, Emma Lundberg, Kalle Jonasson, Mattias Forsberg, Martin
676 Zwahlen, Caroline Kampf, Kenneth Wester, Sophia Hober, Henrik Wernerus, Lisa Björling, and Fredrik
677 Ponten. Towards a knowledge-based human protein atlas. *Nature Biotechnology*, 28(12):1248–1250, 2010.
- 678 Bartlomiej Waclaw, Ivana Bozic, Meredith E Pittman, Ralph H Hruban, Bert Vogelstein, and Martin A
679 Nowak. A spatial model predicts that dispersal and cell turnover limit intratumour heterogeneity. *Nature*,
680 525(7568):261–264, 2015.
- 681 Caroline J Watson, AL Papula, Gladys YP Poon, Wing H Wong, Andrew L Young, Todd E Druley, Daniel S
682 Fisher, and Jamie R Blundell. The evolutionary dynamics and fitness landscape of clonal hematopoiesis.
683 *Science*, 367(6485):1449–1454, 2020.
- 684 Duncan J Watts and Steven H Strogatz. Collective dynamics of small world networks. *Nature*, 393(6684):
685 440–442, 1998.
- 686 Bernard M Waxman. Routing of multipoint connections. *IEEE journal on selected areas in communications*,
687 6(9):1617–1622, 1988.
- 688 Michael C Whitlock and Richard Gomulkiewicz. Probability of fixation in a heterogeneous environment.
689 *Genetics*, 171(3):1407–1417, 2005.
- 690 Sewall Wright. Isolation by distance. *Genetics*, 28(2):114, 1943.

691 Mingfu Wu, Hyog Young Kwon, Frederique Rattis, Jordan Blum, Chen Zhao, Rina Ashkenazi, Trachette L
692 Jackson, Nicholas Gaiano, Tim Oliver, and Tannishtha Reya. Imaging hematopoietic precursor division
693 in real time. *Cell stem cell*, 1(5):541–554, 2007.

694 Lev A Zhivotovsky and Marcus W Feldman. Heterogeneous selection in subdivided populations. *Journal of*
695 *mathematical biology*, 31(7):747–759, 1993.

696 **Acknowledgments**

697 We gratefully acknowledge support from the NIH National Institute of General Medical Sciences (award
698 no. R35GM147445 to OC), the United States-Israel Binational Science Foundation (award no. 2019266 to
699 OC) and from the NIH T32 training grant (no. T32 EB009403 to YPK). We also thank Daniel Couto for
700 help with the bone marrow imaging dataset used in the study. This research was done using computational
701 resources provided by the Open Science Grid, which is supported by the National Science Foundation award
702 1148698, and the U.S. Department of Energy’s Office of Science.

703 **Author Contributions Statement**

704 Y.P.K. and O.C. conceived the study and wrote the manuscript. XXXX

705 **Competing Interests Statement**

706 The authors declare no competing interests.

707 **Additional information**

708 **Supplementary information** The online version contains supplementary material available at XXX.

709 List of Figures

- 710 Figure 1. **Illustration of the population birth death process update rules and graph rewiring**
711 **methods.** **Panel A** illustrates both the dB (death-Birth) and the Bd (Birth-death) update
712 rules. In **Panel B**, we use principle component analysis on 6 graph characteristics (mean, vari-
713 ance, third moment, modularity, average clustering, and assortativity) to highlight the network
714 families studied, as well as the trajectories between them. Each graph family shows clustering
715 using the first three principle components (that explain 89% of the variance in PC space). The
716 black line represents the trajectory in PC space as we rewire graphs starting from preferential
717 attachment (PA) graphs, through power law cluster networks (PLC) and uniform random geo-
718 metric graphs, to normal random geometric graphs (RGG). **Panel C** illustrates the edge swap
719 operation used to tune graph characteristics. At first, there are no edges connecting nodes of de-
720 gree 3 to nodes of degree 4. Two edges are randomly selected to be disconnected and nodes that
721 were "parallel" with respect to the two disconnected edges are then connected, thus preserving
722 the number of edges. After the rewiring step, there are two edges connecting nodes of degree 3
723 to nodes of degree 4, and there is no longer a 4-clique. The degrees of the nodes, however, are
724 preserved.
- 725 Figure 2. **Role of the first moments of the degree distribution on evolutionary dynamics.** The
726 dots represent ensemble averages across 10^6 replicate Monte Carlo simulations, while
727 the lines represent our analytical approximations. **Panels A and C:** We plot the probabilities
728 and times to fixation as a function of the mean of the degree distribution. We use preferential
729 attachment PA graphs, graph size $N = 1000$ and $N_s = 10$. **Panels C and D:** We plot the
730 probabilities and times to fixation as a function of the variance of the degree distribution, while
731 keeping mean degree constant, as in the legend. Here, graphs are PA graphs, $N = 100$ and
732 $N_s = 5$. Probability and time to fixation for well-mixed model are calculated using methods
733 outlined in (Ewens, 2004) (see the Analytic description subsection).
- 734 Figure 3. **Probabilities of fixation across graph families.** The fixation probability is shown on the y-
735 axis as we vary the evolutionary quantity α on the x-axis. The dots represent ensemble
736 averages across 10^6 replicate Monte Carlo simulations, while the lines represent our analytical
737 approximations. Here, graph size $N = 1000$ and $N_s = 10$. Each dot represents simulations
738 on a distinct graph. The various colors represent graphs generated using different generation
739 algorithms. **Panel A** shows results for the death-Birth process. **Panel B** shows results for the

- 740 Birth-death process.
- 741 **Figure 4. Effects of the mixing pattern on the Bd probability of fixation.** The dots represent
742 represent ensemble averages across $5e6$ replicate Monte Carlo simulations, while the lines rep-
743 resent our analytical approximations. Here the degree distribution is held constant as we vary
744 the mixing pattern of the graphs, $N = 100$ and $s = 0.1$. Colors indicate the graph family (with
745 the same degree distribution) as in the legend. Mixing pattern of the graph is tuned using edge
746 swapping operations. To highlight that mean and variance in degree is not enough to predict
747 probabilities of fixation, **Panel A** shows that the probability of fixation can span a wide range
748 of values, for the same mean and standard deviation in degree. **Panel B** shows the dependence
749 of the amplification parameter on the mixing pattern, or correlation in degree r . **Panel C** shows
750 that the selection amplification factor from equation (10) explains the effect of graph mixing
751 pattern on the probability of fixation.
- 752 **Figure 5. Detour and star graphs are graph families that minimize and maximize of prob-**
753 **ability of fixation under under the Bd process.** The dots represent represent ensemble
754 averages across 10^6 replicate Monte Carlo simulations, while the lines represent our analytical
755 approximations. Detour graphs are the strongest suppressors under weak selection. Detour
756 graph consists of a completely connected central cluster and a cycle part. In **Panel A**, we
757 plot the probability of fixation on detour graphs with varying lengths of the detour cycle. Here
758 $s = 0.002$. In **Panel B**, we plot the probability of fixation across graph types, with respect to
759 population size, to illustrate how the star and detour graphs represent extreme values of the
760 fixation probability. Here $s = 0.005$. The two graphs illustrated are detour graphs with different
761 detour lengths.
- 762 **Figure 6. The spatial networks of the hematopoietic stem cell (HSC) populations.** We use a
763 public dataset of spatial locations in the bone marrow consisting of HSC locations (source data:
764 (Coutu et al., 2018)) and proxy niche component locations (source data: (Gomariz et al., 2018)).
765 In **Panel A**, color dots represent an example of the spatial locations of stem cells in the cell
766 population, while the colors corresponds to the density of cells. We show an example of the
767 spatial distribution of hematopoietic stem cells in the mouse tibia: the xy cross-section of the
768 tibia with cells counted in a $260 \mu\text{m} \times 350 \mu\text{m}$ area and the yz cross-section of the tibia with cells
769 counted in a $350 \mu\text{m} \times 11.5 \mu\text{m}$ area. Using this data, we build the resulting geometric random
770 graphs (the cut-off radius of the illustration is set to $300 \mu\text{m}$ for illustration purposes). In **Panel**

771 **B** and **C**, we use these networks to study evolutionary dynamics on these stem cell niche spatial
772 networks as a function of their population size. Here, the diaphysis is the shaft or central part
773 of the tibia and the metaphysis is the neck portion of the bone (source data: (Gomariz et al.,
774 2018)).The color dots use a cut-off distance of 15. Here, $s = 0.01$ and Ns varies with population
775 size. **Panel B** shows results using the Birth-death process and **Panel C** shows the death-Birth
776 process. Dots are averaged over at least 1 million simulations.

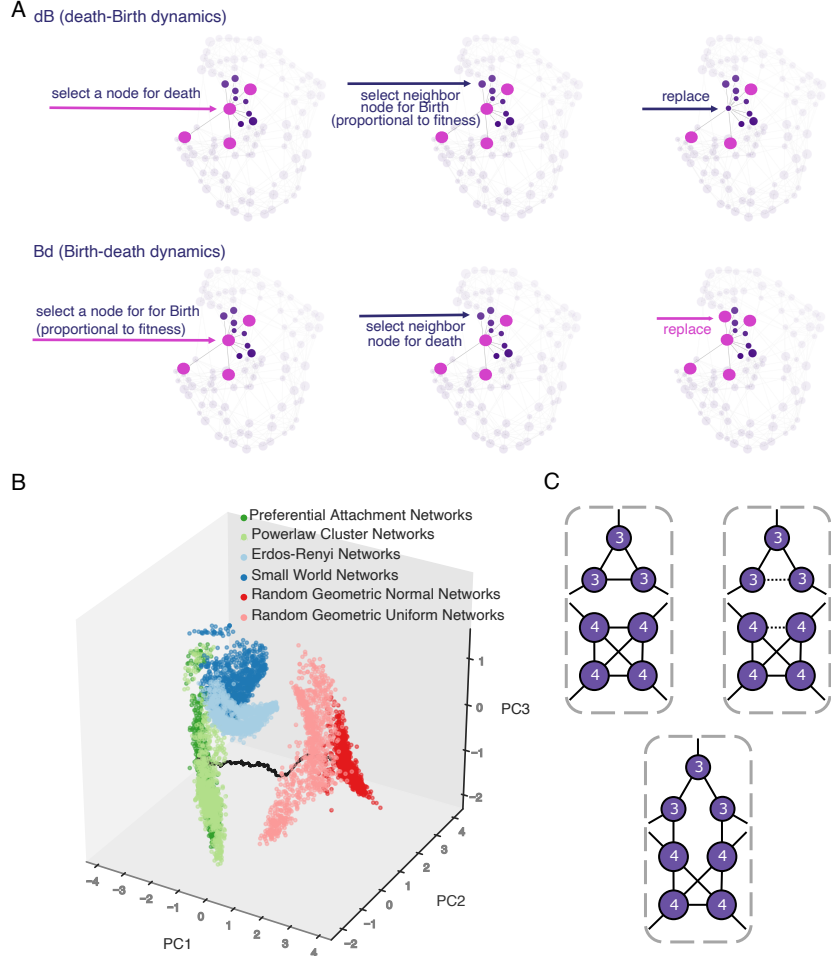


Figure 1: Illustration of the population birth death process update rules and graph rewiring methods. **Panel A** illustrates both the dB (death-Birth) and the Bd (Birth-death) update rules. In **Panel B**, we use principle component analysis on 6 graph characteristics (mean, variance, third moment, modularity, average clustering, and assortativity) to highlight the network families studied, as well as the trajectories between them. Each graph family shows clustering using the first three principle components (that explain 89% of the variance in PC space). The black line represents the trajectory in PC space as we rewire graphs starting from preferential attachment (PA) graphs, through power law cluster networks (PLC) and uniform random geometric graphs, to normal random geometric graphs (RGG). **Panel C** illustrates the edge swap operation used to tune graph characteristics. At first, there are no edges connecting nodes of degree 3 to nodes of degree 4. Two edges are randomly selected to be disconnected and nodes that were "parallel" with respect to the two disconnected edges are then connected, thus preserving the number of edges. After the rewiring step, there are two edges connecting nodes of degree 3 to nodes of degree 4, and there is no longer a 4-clique. The degrees of the nodes, however, are preserved.

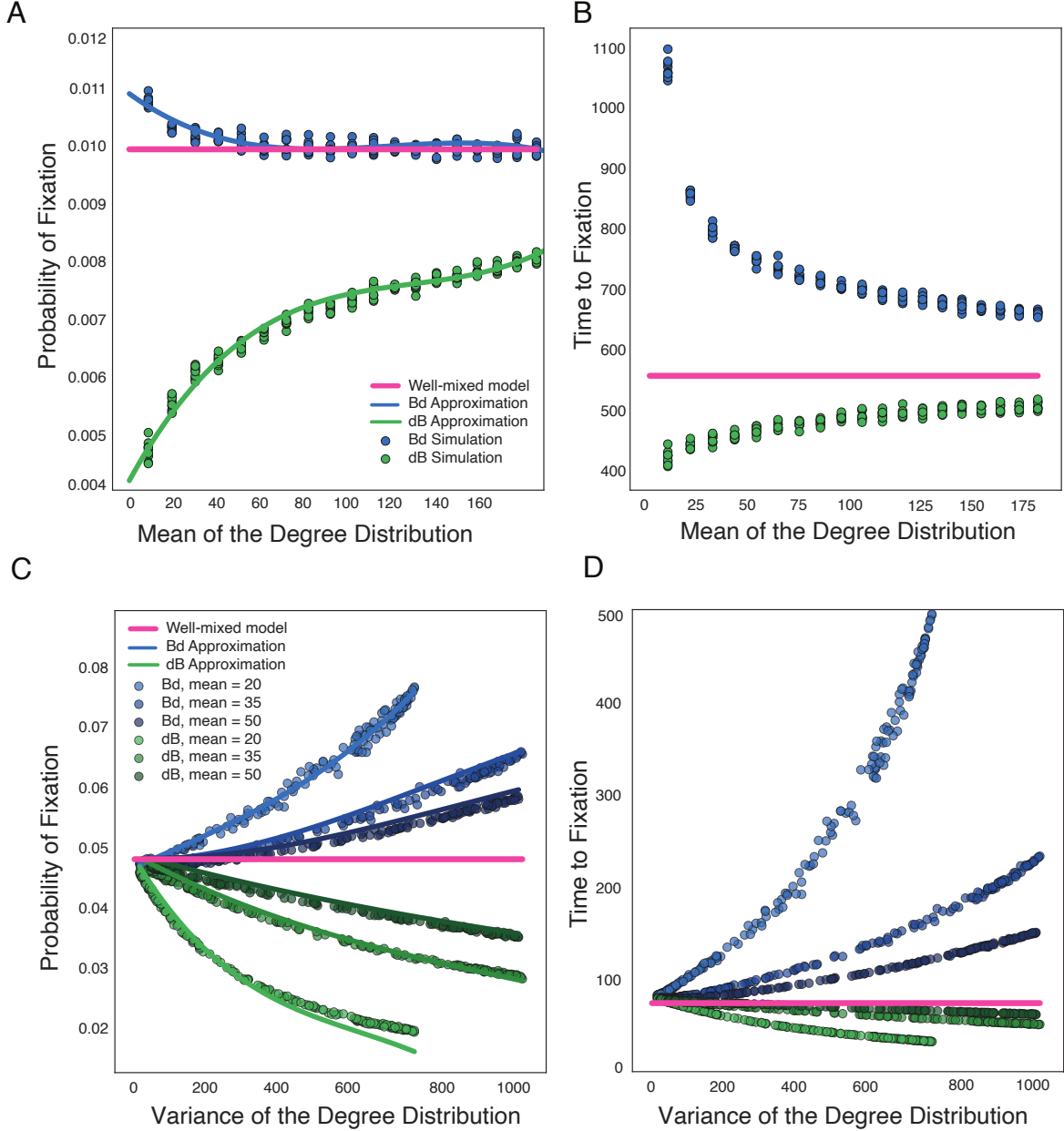


Figure 2: Role of the first moments of the degree distribution on evolutionary dynamics. The dots represent ensemble averages across 10^6 replicate Monte Carlo simulations, while the lines represent our analytical approximations. **Panels A and C:** We plot the probabilities and times to fixation as a function of the mean of the degree distribution. We use preferential attachment PA graphs, graph size $N = 1000$ and $N_s = 10$. **Panels C and D:** We plot the probabilities and times to fixation as a function of the variance of the degree distribution, while keeping mean degree constant, as in the legend. Here, graphs are PA graphs, $N = 100$ and $N_s = 5$. Probability and time to fixation for well-mixed model are calculated using methods outlined in (Ewens, 2004) (see the Analytic description subsection).

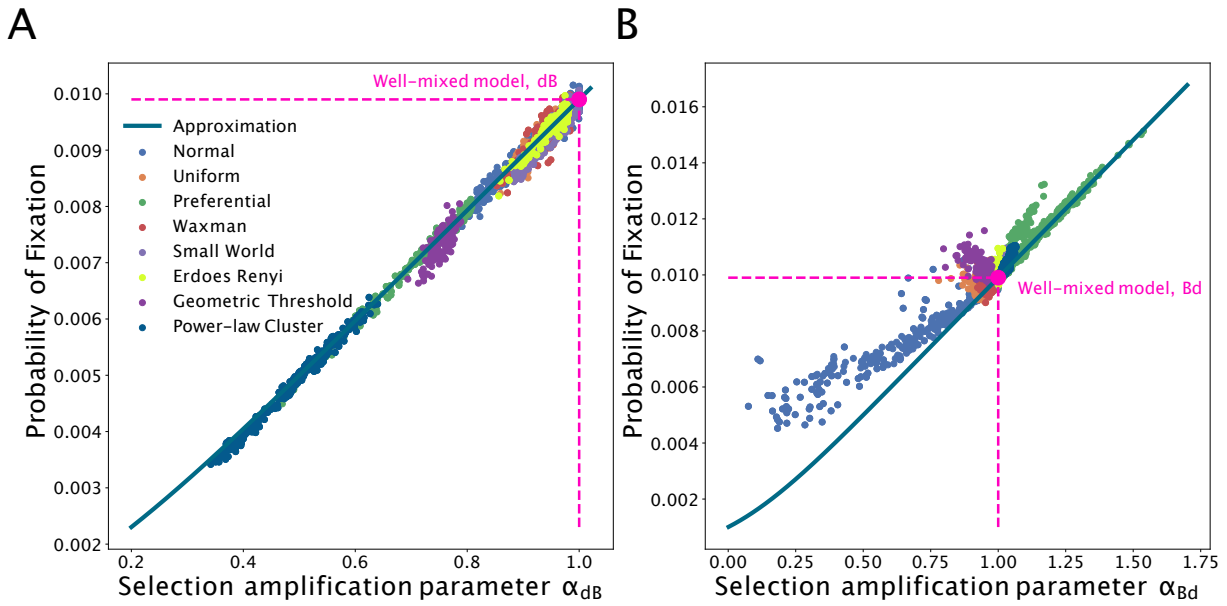


Figure 3: **Probabilities of fixation across graph families.** The fixation probability is shown on the y-axis as we vary the evolutionary quantity α on the x-axis. The dots represent ensemble averages across 10^6 replicate Monte Carlo simulations, while the lines represent our analytical approximations. Here, graph size $N = 1000$ and $N_s = 10$. Each dot represents simulations on a distinct graph. The various colors represent graphs generated using different generation algorithms. **Panel A** shows results for the death-Birth process. **Panel B** shows results for the Birth-death process.

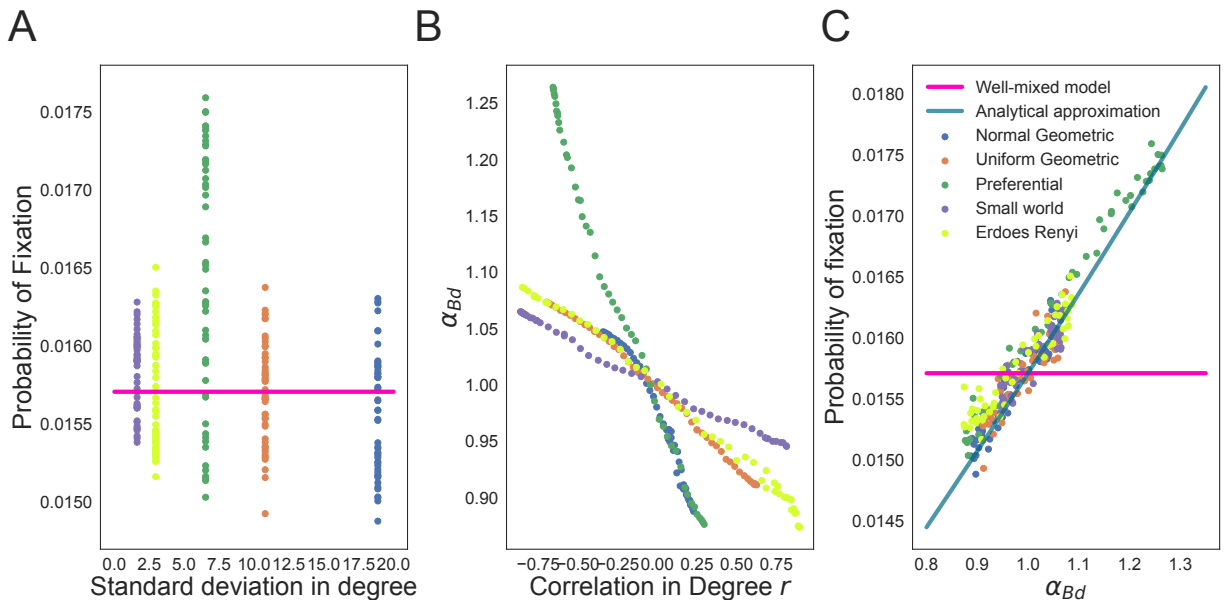


Figure 4: **Effects of the mixing pattern on the B_d probability of fixation.** The dots represent ensemble averages across $5e6$ replicate Monte Carlo simulations, while the lines represent our analytical approximations. Here the degree distribution is held constant as we vary the mixing pattern of the graphs, $N = 100$ and $s = 0.1$. Colors indicate the graph family (with the same degree distribution) as in the legend. Mixing pattern of the graph is tuned using edge swapping operations. To highlight that mean and variance in degree is not enough to predict probabilities of fixation, **Panel A** shows that the probability of fixation can span a wide range of values, for the same mean and standard deviation in degree. **Panel B** shows the dependence of the amplification parameter on the mixing pattern, or correlation in degree r . **Panel C** shows that the selection amplification factor from equation (10) explains the effect of graph mixing pattern on the probability of fixation.

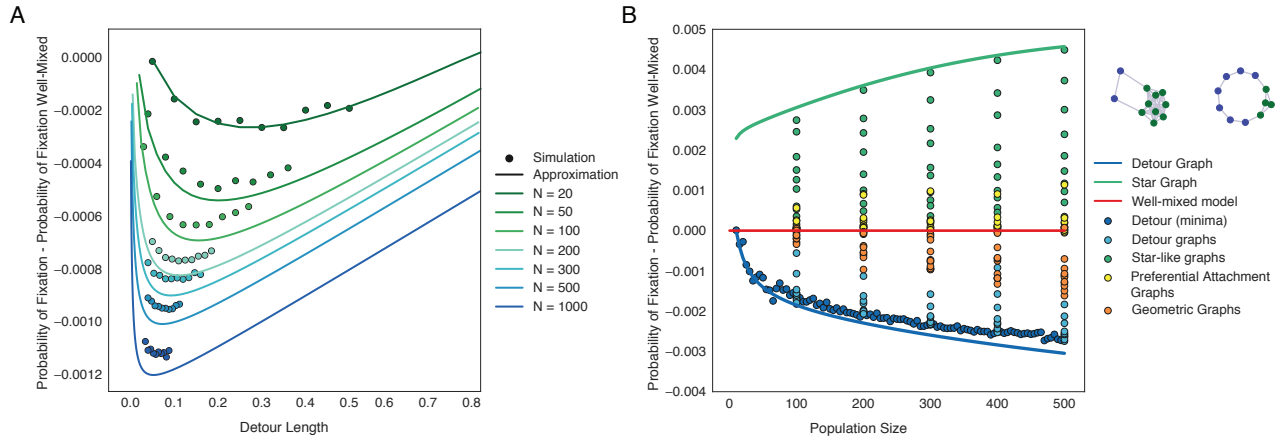


Figure 5: Detour and star graphs are graph families that minimize and maximize of probability of fixation under the Bd process. The dots represent ensemble averages across 10^6 replicate Monte Carlo simulations, while the lines represent our analytical approximations. Detour graphs are the strongest suppressors under weak selection. Detour graph consists of a completely connected central cluster and a cycle part. In **Panel A**, we plot the probability of fixation on detour graphs with varying lengths of the detour cycle. Here $s = 0.002$. In **Panel B**, we plot the probability of fixation across graph types, with respect to population size, to illustrate how the star and detour graphs represent extreme values of the fixation probability. Here $s = 0.005$. The two graphs illustrated are detour graphs with different detour lengths.

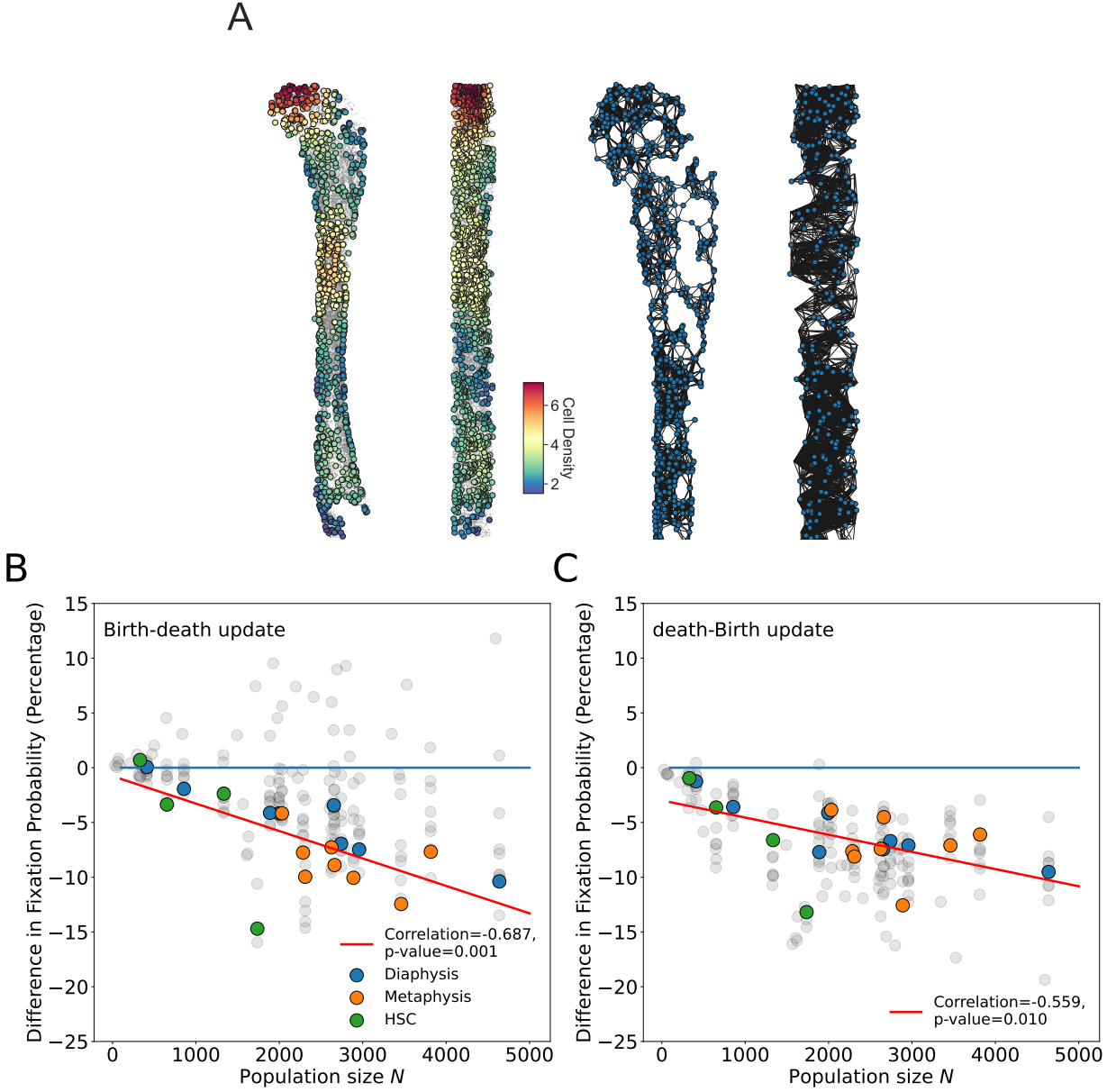


Figure 6: The spatial networks of the hematopoietic stem cell (HSC) populations. We use a public dataset of spatial locations in the bone marrow consisting of HSC locations (source data: (Coutu et al., 2018)) and proxy niche component locations (source data: (Gomariz et al., 2018)). In **Panel A**, color dots represent an example of the spatial locations of stem cells in the cell population, while the colors corresponds to the density of cells. We show an example of the spatial distribution of hematopoietic stem cells in the mouse tibia: the xy cross-section of the tibia with cells counted in a $260\ \mu\text{m} \times 350\ \mu\text{m}$ area and the yz cross-section of the tibia with cells counted in a $350\ \mu\text{m} \times 11.5\ \mu\text{m}$ area. Using this data, we build the resulting geometric random graphs (the cut-off radius of the illustration is set to $300\ \mu\text{m}$ for illustration purposes). In **Panel B** and **C**, we use these networks to study evolutionary dynamics on these stem cell niche spatial networks as a function of their population size. Here, the diaphysis is the shaft or central part of the tibia and the metaphysis is the neck portion of the bone (source data: (Gomariz et al., 2018)). The color dots use a cut-off distance of 15. Here, $s = 0.01$ and Ns varies with population size. **Panel B** shows results using the Birth-death process and **Panel C** shows the death-Birth process. Dots are averaged over at least 1 million simulations.